Flow plane orientation in the upper mantle under the Western/Central United States from SKS shear-wave splitting observations

Eric Löberich[1] and Götz Bokelmann[1]

[1] *Department of Meteorology and Geophysics, University of Vienna, Vienna, Austria*

SUMMARY

The causes of seismic anisotropy are still under debate. In particular it is important to understand the extent to which seismic anisotropy is due to more recent geodynamic activities in the asthenosphere, or to frozen-in deformation in the lithosphere. We show that these two endmember cases can in principle be distinguished using shear-wave splitting observations from SKS waves. This is illustrated by the simple example of pure olivine with horizontal a-axis, and differing orientations of the other two axes, namely vertical b and vertical c. The azimuthal dependence of shear-wave splitting measurements is described by two parameters, which can provide additional information about subsurface deformation. In particular the oscillation parameter d_1 constrains the orientation of foliation. We demonstrate that shear-wave splitting in the Western and Central United States indeed shows the predicted azimuthal dependence, related to a mainly subhorizontally-oriented flow plane of deformation in the upper mantle. This has important implications for asthenospheric flow.

Key words: Seismic anisotropy, Numerical approximations and analysis, Mantle processes, Rheology: mantle, Dynamics of lithosphere and mantle, North America

1 INTRODUCTION

Seismic anisotropy, as manifest in the directional dependence of phase velocities and polarization (e.g., Mainprice 2015), arises from preferred orientation of structural features in the Earth, at a spatial scale smaller than the wavelength. In the mantle, it is thought to be mainly caused by lattice-prefered orientation of minerals, i.e. olivine and orthopyroxene (Nicolas & Christensen 1987; Babuska & Cara 1991; Karato 2008; Mainprice 2015, and references therein).

A common way to quantify azimuthal anisotropy in the upper mantle is to use shear-wave splitting (SWS) measurements. That approach goes back to the discovery of unexpected energy on the transverse component of SKS arrivals, which is not supposed to occur in an isotropic medium (Vinnik et al. 1984; Silver & Chan 1988). A planar S-wave passing through an anisotropic medium will split into two quasi-S-waves (qS) with mutually-perpendicular polarization, similar to the well-known birefringence in optics. Their seismic velocities are generally different, which leads to a separation of the two qS-waves along the ray path, in space and in time. Analysing seismic recordings, the delay time (Δt) between the two can be derived, as well as the orientation of the faster wave (ϕ)(Vinnik et al. 1989; Silver & Chan 1991). The most convenient seismological phase for such studies is SKS, since source-side anisotropy effects along the ray path are eliminated. However, the resolution in depth is relatively weak, leaving open questions as to the depth region of the anisotropy and the related mechanism.

Nevertheless, the use of seismic anisotropy in general, and SWS in particular, has had much impact on understanding subsurface deformation. Spatially coherent patterns of SWS parameters have been found in many regions, e.g. a mountain-chain-parallel alignment of ϕ along the Alpine Belt (Barruol et al. 2011; Bokelmann et al. 2013; Qorbani et al. 2015) or the trench-perpendicular orientation of ϕ in the Cascadia Subduction Zone (e.g. Long & Silver 2008; Eakin et al. 2010). As interesting as SWS is, its interpretation would be much stronger if the orientation of rock foliation in the subsurface could be determined (Fig. 1), since rock foliation gives an indication of the orientation of the flow plane. The two can often be assumed to be parallel to each other (e.g. Bokelmann 2002a,b, and references therein). It has so far seemed impossible to determine the orientation of the foliation (and flow) plane from SKS splitting. That ambiguity has led to major debates in the community, e.g. about the proper interpretation of seismic anisotropy in cratonic regions. For those regions, Vinnik et al. (1989) and Savage & Silver (1993) have argued that the observed anisotropy is caused by Simple Asthenospheric Flow (SAF), while Silver & Chan (1988, 1991) have concluded that the foliation plane is rather due to Vertically-Coherent Deformation (VCD) (fossil deformation left over from the creation of continental lithosphere).

In this paper we show that assuming a vertical arrival of SKS phases, as in the standard SWS approach, leads to loss of useful information. The fact that upper mantle incidence angles of SKS phases are around $10\,°$ from the vertical has already proven useful, e.g in the study of Song & Kawakatsu (2012). Taking the non-vertical incidence into account induces an azimuthal variation of SWS parameters. Interestingly, the angular variation is different for the two cases SAF and VCD. This will be demonstrated in the next section, following a solution of the Christoffel equation by Davis (2003). Later we will apply the new technique to a SWS dataset from Western and Central US, and show how the new constraint can be used to extract more information about seismic anisotropy and subsurface deformation, in particular to infer the orientation of the flow plane in the subsurface. This allows to better understand the origin of upper mantle anisotropy.

2 METHOD

2.1 Near-vertical SWS approach

The propagation of elastic waves (with planar wavefronts) in an anisotropic medium is governed by the Christoffel equation

$$\rho v_s^2 = C_{ijkl}\nu_j\nu_k s_i s_l. \tag{1}$$

We assume a homogeneous anisotropic (orthorhombic) medium, characterized by the density ρ and stiffness tensor C. The reference case is that of a vertically arriving SKS phase, which has a propagation direction ν and polarization direction s, described by $[\nu_1,\, \nu_2,\, \nu_3] = [0,\, 0,\, 1]$ and $[s_1,\, s_2,\, s_3] = [\cos(\phi),\, \sin(\phi),\, 0]$. In this situation the SWS fast orientation azimuths ϕ_0 can be calculated as

$$\phi_0 = \frac{1}{2}\tan^{-1}\left(\frac{2C_{2313}}{C_{1313} - C_{2323}}\right) \tag{2}$$

and from $C_{2313} = 0$ follows $\phi_0 = 0$. Consequently the delay time Δt_0 is defined by

$$\Delta t_0 = D\left(\frac{1}{v_{ss}} - \frac{1}{v_{sf}}\right), \tag{3}$$

with

$$v_{sf} = \sqrt{\frac{C_{1313}}{\rho}} \text{ and } v_{ss} = \sqrt{\frac{C_{2323}}{\rho}}. \tag{4}$$

Here the parameters v_{sf} and v_{ss} represent the fast and slow phase velocity, while the path length is indicated by D. As the actual incidence angle θ is around $10\,^\circ$ at upper mantle depths, the propagation direction is then $[\nu_1, \nu_2, \nu_3] = [\sin(\theta)\cos(z), \sin(\theta)\sin(z), \cos(\theta)]$, where z denotes the azimuth. Simplified analytical expressions for fast orientation and delay time can be obtained using a Taylor-series expansion if $\theta < 30\,^\circ$. Considering the projection of the fast axis onto the horizontal plane, and the angle β, which this projection makes with respect to the x_1 coordinate-axis, the polarization orientation can be assumed to have $s_2 = s_1\tan(\beta) \approx s_1\beta$, from which follow

$$s_1 = \frac{1}{\sqrt{\left[1 + \beta^2 + \left(\frac{-\nu_1 - \beta\nu_2}{\nu_3}\right)^2\right]}} \text{ and } s_3 = -\frac{(\nu_1 s_1 + \nu_2 s_1 \beta)}{\nu_3}. \tag{5}$$

The fast orientation is then

$$\phi = \phi_0 + \delta\phi, \tag{6}$$

with

$$\delta\phi = d_1 \sin(2z)\theta^2. \tag{7}$$

This describes an oscillation around ϕ_0 with $180\,^\circ$ periodicity for varying azimuth z (and incidence angle θ). d_1 is the "oscillation parameter", where $d_1 = -f1/f4$, is given by

$$\begin{aligned} f_1 &= C_{1212} - C_{2233} - C_{1133} - 2C_{1313} + C_{1122} - C_{2323} + C_{3333} \text{ , and} \\ f_4 &= -2C_{1313} + 2C_{2323}. \end{aligned} \tag{8}$$

Similarly, also the delay time is found to show oscillations around Δt_0 as

$$\Delta t = \Delta t_0 + e_1\theta^2 + \delta\Delta t, \tag{9}$$

with

$$\delta\Delta t = e_2\cos(2z)\theta^2. \tag{10}$$

Here

$$e_1 = \frac{D}{2}\sqrt{\frac{\rho}{c^3}}\,(F_1 - S_1) \text{ and } e_2 = \frac{D}{2}\sqrt{\frac{\rho}{c^3}}\,(F_2 - S_2) \tag{11}$$

are related to

$$
\begin{aligned}
F_1 &= -\frac{5}{2}C_{1313} - C_{1133} + \frac{1}{2}C_{1111} + \frac{1}{2}C_{3333} + \frac{1}{2}C_{1212} \\
F_2 &= -\frac{3}{2}C_{1313} - C_{1133} + \frac{1}{2}C_{1111} + \frac{1}{2}C_{3333} - \frac{1}{2}C_{1212} \\
S_1 &= -\frac{5}{2}C_{2323} - C_{2233} + \frac{1}{2}C_{2222} + \frac{1}{2}C_{3333} + \frac{1}{2}C_{1212} \\
S_2 &= \frac{3}{2}C_{2323} + C_{2233} - \frac{1}{2}C_{2222} - \frac{1}{2}C_{3333} + \frac{1}{2}C_{1212} \\
&\text{and } \bar{c} = \sqrt{C_{1313}C_{2323}}.
\end{aligned}
\tag{12}
$$

2.2 Predicted shear-wave splitting parameters

Figure 1 (left) shows the expected ray geometry for SKS, propagating through the upper mantle along a cone with around 10° incidence angle. It also presents the two endmember models of geodynamic interest (center), SAF (top) and VCD (bottom), which are associated with different orientations of the foliation plane (see Silver 1996, and references therein). As olivine is the main source of seismic anisotropy in the upper mantle, we illustrate the new observational constraint by considering an idealised case of pure olivine. If deformation occurs by dislocation creep (Nicolas & Christensen 1987), the a-axes would be aligned subhorizontally. We thus take a single olivine crystal, with a horizontal a-axis, and consider the orientation of a vertical b-axis (b-up), and a vertical c-axis (c-up). These two orientations represent, for the moment, the SAF model (b-up), and the VCD model (c-up).

In the calculations of the expected azimuthal variations of SWS parameters for Fig. 1 (see Appendix A), we use the elastic constants from the San Carlos olivine of Abramson et al. (1997) (see also the MATLAB toolbox for quantitative texture analysis (MTEX) of Hielscher & Schaeben 2008) and apply functions of the MATLAB seismic anisotropy toolbox (MSAT) (Walker & Wookey 2012). Since the occurrence of e.g. orthopyroxene, clinopyroxene and pyrope in the upper mantle would further influence the observed SWS parameters, we determine the Voigt-Reuss-Hill average (e.g. Mainprice et al. 2000), to reduce the amount of olivine. Following McDonough & Rudnick (1998), upper mantle lherzolite can consist of up to approximately 70 % olivine. For simplicity we assume this amount to be aligned in a b-up or c-up orientation, while 30 % remain randomly oriented (isotropic equivalent). The oscillation parameter d_1, as well as the e_1 and e_2 parameters are calculated for an incidence angle θ of $\sim 11.23^\circ$ and a path length of $D \sim 101.59\,\mathrm{km}$ (as given in a reference MSAT routine from Wookey & Walker 2015a). Complementary the influence of the amount of olivine on d_1 and e_2 is shown in Appendix B in relation to the changing strength of anisotropy.

Comparing the two orientations (right) we note that the Δt variation is somewhat similar, but the amplitudes, related to the e_2 values ($e_{2b} \sim 3.61$, $e_{2c} \sim 5.32$), differ. A much stronger difference is apparent for ϕ. Their oscillations have similar size, but the polarity is flipped. That is also apparent from the opposing values of the oscillation parameter d_1 ($d_{1b} \sim -0.7$, $d_{1c} \sim 0.51$), which are calculated directly from the stiffness tensors. This indicates that it may be possible to use backazimuthal variations of ϕ at a station to determine the orientation of the foliation plane in the subsurface.

3 DATA, ANGULAR DISTRIBUTION, AND RESULTS

Since the amplitude of oscillations are generally smaller than expected mean measurement uncertainties per station, a larger number of measurements is required to extract this effect from observations. An investigation of a dense array is thus of advantage, as well as searching for spatial average properties only, rather than detailed spatial variations.

A suitable test dataset is SWS-DB-MST, which was provided by Liu et al. (2014) (see Fig. 2). It contains SWS measurements from PKS and SKS and SKKS arrivals, recorded between the years 1989 - 2012 on 1774 broadband stations of various networks in the US, including IRIS/USGS Global Seismographic Network (IU) and US National Seismic Network (US), as well as USArray Transportable Array (TA), PASSCAL (P) and GEOSCOPE (G). Overall, there are 16105 measurements (12247 SKS, 2451 SKKS, 1407 PKS) in the dataset. Fast orientations vary spatially, while their average agrees with North America's absolute plate motion direction (e.g. Liu et al. 2014; Hongsresawat et al. 2015).

To analyze the dataset, we first select the SKS and SKKS phases (in the following we will refer to these simply as SKS) and transfer the ϕ interval from $[-90\,^\circ, 90\,^\circ]$ to $[0\,^\circ, 180\,^\circ]$. Figure 3 shows the statistical distribution of ϕ (top left), Δt (bottom left), and the related mean standard deviation $\overline{\sigma}$ per station (right). To ensure a higher stability of averaged values (circular operations are computed using the Circular Statistics Toolbox (CircStat) from Berens 2009), $\overline{\sigma}$ is determined for stations with at least five measurements. All four quantities unveil a unimodal distribution, whereby ϕ is mainly oriented ENE - WSW and the number of measurements for Δt peaks at the 1.2 s interval. Considering individual stations, ϕ and Δt show an average uncertainty of $\sim 8\,^\circ$ and 0.2 s - 0.3 s respectively (for further reading see Liu et al. 2014).

Continuing with the data analysis Fig. 4 (left) shows a wide spread in the related backazimuthal distribution of ϕ (top) and Δt (bottom), reflecting the diversity of anisotropy at large scale, which was also apparent in Fig. 2, as the spatial change of ϕ. Beside the spread an uneven distribution of earthquakes is unveiled. Individual measurements accumulate especially within backazimuth ranges of 0 to 45 ° and 225 to 360 °. The latter range holds the highest concentration of data points. SWS measurements between $\sim$ 45 ° - 225 ° are much less present. Our study is thus azimuthally biased by the unequal occurrence of earthquakes. The distribution of ϕ as a function of backazimuth further provides a simple test of any SWS dataset. Since the amplitude of the transverse-component signal is zero for backazimuths from either fast or slow direction, no SWS is indeed observed (top left, magenta lines) for backazimuths parallel or perpendicular to the fast orientation (Null events) (e.g. Wüstefeld & Bokelmann 2007; Wüstefeld et al. 2008).

To be able to investigate different stations jointly, searching for possible trends in the backazimuthal distribution, we calculate the variation $\delta\phi$ and $\delta\Delta t$ of each individual SWS measurement with respect to $\overline{\phi}$ and $\overline{\Delta t}$, the corresponding means per station. Thereby only stations with at least five SWS measurements are selected to ensure a more stable calculation of the mean. In the transferred range of ϕ, we define $\delta\phi$ as the smallest angle with $\overline{\phi}$, leading to a codomain $[-90\,°, 90\,°]$. Different $\overline{\phi}$ shift the expected oscillations also along the backazimuth (right). Assuming ideal single-layer cases of anisotropy for each station across Western and Central United States, this correction would align the data points like as if they came from the same station. This may unveil small variations from the related means that we seek. However, the possible presence of two-layer cases, which could introduce a variation of 90 ° backazimuth periodicity and larger amplitudes, have the potential to overlay the 180 ° effect we are searching for. Also the occurrence of outliers affect the $\overline{\phi}$ calculation. The correction in $\delta\phi$ (top) hence does not lead to a vertical alignment, instead the diagonal gaps are still present.

As the density of data points is sometimes very high, one might overlook a possible variation in $\delta\phi$ and $\delta\Delta t$ (bottom). We therefore determine 2D histograms by subdividing the distributions along both cartesian axes, computing the frequency per bin ($\sim 8.95\,° \times 2.19\,°$ and $\sim 8.95\,° \times 0.04\,\mathrm{s}$) normalized to the maximum per abscissa unit. The relative frequencies reveal that $\delta\phi$ and $\delta\Delta t$ are highly concentrated around 0 ° and 0 s, and give indications for variations of both parameters. As the distribution itself is biased, a comparison with expected oscillations of SWS parameters for b-up and c-up olivine orientation of Fig. 1 (right) might be elusive at this point. To avoid the problem, we first constrain the selection of data points introducing thresholds. Based on the spread of the relative frequencies, the codomain of $\delta\phi$ and $\delta\Delta t$ is limited by the related 5 % and 95 % quantile (right, magenta lines) subsequently, reducing the influence of outliers and more complex anisotropy. To ensure to not artificially change the general behavior of our findings, we further tested different combinations of thresholds, and found that they produce essentially similar results (see Appendix C).

As discussed before, the station-corrected display in Fig. 4 (right) also contains a biased distribution, hence the thresholds in $\delta\phi$ and $\delta\Delta t$ are not restrictive enough to remove outliers. Also the bias needs to be removed. The measurements are most difficult to make at backazimuths parallel or perpendicular to the fast direction. We thus introduce boundaries in the domain and take data points in intervals of $\pm 15^\circ$ around 45°, 135°, etc. These are also the angles, where the difference between b-up and c-up olivine is clearest in $\delta\phi$, and thus most significant to distinguish the SAF and VCD model as shown in Fig. 1 (right, gray shaded intervals). This is less the case for Δt, since the measurements are difficult to make around backazimuths around 0°, 90°, etc.

Figure 5 shows the distribution of relative frequencies (left) inside the intervals of interest (per bin of $0.5^\circ \times 30^\circ$ and $0.02\,\mathrm{s} \times 30^\circ$) of $\delta\phi$ (top) and $\delta\Delta t$ (bottom), and the averages of measurements further within the thresholds in comparison (right) with the expected backazimuthal variations of the upper configuration from Fig. 1 (right), the b-up case. The distributions indicate that the majority of $\delta\phi$ and $\delta\Delta t$ mainly occur around 0° and 0 s, however general shifts in polarity between different intervals are already recognizable in $\delta\phi$. The very good agreement with the expectations become more obvious in the comparison. This corresponds to the case where the main source of observed anisotropy is related to a horizontal orientation of the rock foliation (and flow) plane, which would be in line with subsurface deformation being primarily in the asthenosphere and coherent with the SAF model. To verify the robustness of our findings and the procedure under consideration of the assumptions made, we generate an additional synthetic dataset in Appendix D and apply the method again.

4 DISCUSSION

We have shown that the upper mantle anisotropy from SKS under Western and Central United States shows an azimuthal variation that is consistent with a horizontal orientation of the foliation plane. The corresponding parameters are approx. -0.7 for the oscillation parameter d_1, and 3.61 for e_2.

In this analysis, we have assumed that the seismic anisotropy obeys an orthorhombic symmetry. This seems reasonable, since the major minerals in the depth range of interest, olivine and orthopyroxene, have orthorhombic symmetry (Nicolas & Christensen 1987). In principle, this assumption is not particularly restrictive, since the technique should be applicable (generalizable) also to other crystal symmetries. Only hexagonal (transverse) symmetry would be of particular relevance here. We have assumed that the orientation of the olivine a-axis is horizontal, and have focused on the orientation of the other two axes. The Taylor series approach used in this study appears well-applicable to SKS phases due to their steep incidence near in the upper mantle, both at lithospheric and asthenospheric depth (see Appendix E).

The limited number of measurements has precluded such a study in the early years of seismic anisotropy research. There is a sufficient number of observations nowadays though, to render this new constraint feasible. This can easily be confirmed: with the number of measurements on the order of 10000, the uncertainty should decrease by a factor of 100. This decreases the assumed errors of fast orientations from (the order of) 10° to 0.1°, which is much below the predicted effect. For the splitting delays the error should be 0.01 s rather than 1 s. However, since the backazimuthal range where the effect of non-vertical SWS would be the largest for Δt coincides with possible Null measurements, we cannot inspect the full backazimuthal pattern of splitting delays. In any case, it is clear that the fit between observations and prediction in Fig. 5 (right) is excellent. This fit is all the more remarkable, as we have not adapted the model to the observations. We simplified the reference example of Wookey & Walker (2015a) to a single-layer case, and had no need for any further adapting, since it fits the observations well. We also did not see consistent signs of 2-layer anisotropy, e.g. the typical 90° periodicity, or a 360° dependence in the case of a dipping layer, dominating our analysis on this large scale. Higher complexities have been observed on regional scale (e.g. Menke & Levin 2003; Yuan & Romanowicz 2010; Yang et al. 2014) and hold the potential to bias the small scale variation of SWS parameters. However, selecting only a subset of stations of high-quality and more likely single-layer anisotropy, the agreement between the observed behavior and expected variations of SWS parameters for a b-up olivine case is still good (see Appendix F). We thus consider the findings of Fig. 5 under the assumptions made to be related to the effect of non-vertical SWS arrivals rather than to be controlled by multiple-layer anisotropy. The value of the d_1 parameter for the b-up model (-0.7) can be considered as an average value for Western and Central United States. The splitting delay for that same crystallographic model would be around 1.6 s, as shown for vertical incidence in Fig. 1 (right, black lines). This value is indeed close to the average of the observations that have entered this study.

It is interesting to relate this result to observed orientations of crystals in xenoliths (as reported e.g. in Nicolas & Christensen 1987). Figure 6 shows the expected relations between crystal orientation and flow geometry, for a set of temperature domains in the upper mantle. These different olivine slip systems all give rise to certain values of the oscillation parameter d_1. Interestingly, the only slip system that predicts the observed negative value, is the second mechanism from the top (the "high-temperature mechanism"). All other mechanisms would give rise to a value close to zero; in those cases, different oscillation parameters average out to near-zero.

We can thus confirm that b-axes are preferentially oriented vertically for our study region. This suggests that the high-temperature mechanism of olivine deformation is responsible for the observed anisotropy. The most likely environment in which it has been created is the asthenosphere, so following the SAF model, foliation planes are horizontally aligned, as is the slip plane. Whether the lithosphere further contributes to that is a matter of interpretation and remains a target of future studies.

It is important to keep in mind though that the region of study contained only a small portion of the craton area, and the b-up case found here may thus not be characteristic for cratonic areas, as studies have indicated before (e.g. Bokelmann & Silver 2000, and referenes therein). Xenolith samples from the upper mantle sometimes show a girdle configuration, e.g. a random distribution of b- and c-axes (e.g. Soustelle et al. 2010) around the a-axis (see e.g. the medium- or low-temperature mechanism in Fig. 6). If a girdle fabric were prevalent also in the Western and Central United States we would obtain an average of the two configurations in Fig. 1, and thus a rather weak azimuthal variation of fast orientation (an order of magnitude smaller) but this is in contrast with the observations in Fig. 5.

Our study is in agreement with radial anisotropy obtained from surface waves, e.g. the study of Yuan et al. (2011), who find a depth region with predominantly positive radial anisotropy ($V_{sh} > V_{sv}$) down to 200 km depth. The SKS splitting data are thus consistent with the anisotropy caused by asthenospheric flow. Similar conclusions have been made by a number of studies before. The agreement (on average) with absolute plate motion direction (Liu et al. 2014; Hongsresawat et al. 2015) is indicative, but not enough for a firm conclusion. In any case, there are strong deviations from that direction with the most striking one being the circumferential pattern in the Great Basin (e.g. Özalaybey & Savage 1995; Savage & Sheehan 2000; Eakin et al. 2010; Yuan & Romanowicz 2010, and refererences therein). The orientation of flow in the mantle is strongly influenced by regional features, lithospheric topography, mantle upwelling etc. (Savage & Sheehan 2000; Hongsresawat et al. 2015).

It is an interesting question to ask what the percentage of olivine below the Western and Central United States is. We have followed McDonough & Rudnick (1998) who stated a variety of different mantle compositions. Depending whether a primitive mantle, massif, or a situation off-craton is considered, the overall amount of olivine can be assumed between $56 - 62\%$ in a spinel peridotite facies and around $57 - 68\%$ in a garnet peridotite facies. A more recent study of Faccenda & Capitanio (2013) considered 70% of olivine in their modeling. As an initial guess, we used that later value, and further simplified that these 70% are aligned in the same orientation, while the remaining 30% are distributed randomly (isotropic). This already explained the actual variation of the mean and median of $\delta\phi$ well. However, Davis (2003) for example used another olivine stiffness tensor and only assumed 30% of olivine to be aligned, but still the d_1 value was determined to be -0.57 and 0.53 in a b-up and c-up situation, what is comparable to the -0.7 and 0.51 we calculated. Appendix B further confirms that the effect of changing the aligned olivine percentage is small in d_1. Our investigation does not include orthopyroxene and other crystal types constituting the upper mantle, as the data are already fit by the simple model. Adding orthorhombic orthopyroxene, and to a much smaller degree monoclinic clinopyroxene and cubic garnet (Nicolas & Christensen 1987; Babuska & Cara 1991; Karato 2008; Mainprice 2015, and references therein) would effectively modify the required layer thickness somewhat. A more important conclusion is though that the high absolute value of d_1 leaves little room for a girdle distribution in the upper mantle.

With the new methodology established, future studies may focus on smaller regions. The different geological provinces of the United States could be investigated separately, directly inverting for the oscillation parameter d_1, and the orientation of the flow plane. Nevertheless, the required large number and broad backazimuthal distribution per station will be a limiting factor, but considering the increased number of stations and the dense coverage due to USArray that seems feasible, at least for some areas. So far we have considered two idealized horizontal single-layer case models, but future studies may include a generalization to multiple- or dipping-layer anisotropy, involving geodynamic modeling to capture the development of lithosphere and asthenosphere. Davis (2003) already derived a more complex version of the Taylor-series expansion, suitable to determine the variation of the fast orientation in a non-vertical incidence scenario for a dipping layer, introducing a 360° periodicity. A generalization of the approach, able to describe the non-vertical SWS behavior in a multiple-layer case, e.g. in addition to the 90° variation expected in a two-layer situation, would probably resort to numerical modeling, based on an extension of the numerical solution of Mainprice (1990), which is comparable to the result of the Taylor-series expansion in a single-layer case (see Appendix A).

5 CONCLUSIONS

In this study we have introduced and tested a new approach to better understand seismic anisotropy in the upper mantle from shear-wave splitting. The approach is based on the non-vertical incidence of SKS waves and yields additional information on subsurface deformation. We have considered two scenarios of upper mantle anisotropy related to a lithospheric or asthenospheric origin, and shown that these two endmember models can be distinguished in real data, by using the backazimuthal variation of SKS splitting measurements. Investigating shear-wave splitting results in the Western and Central United States, the derived variations of individual measurements per station ($\delta\phi, \delta\Delta t$) unveiled the predicted variations, expected from simple asthenospheric flow, and $\delta\phi$ constrained the oscillation parameter. We have also seen that a girdle fabric is unlikely to be a prevalent feature of the upper mantle in the region. This shows that the new approach is promising and encourages future studies at regional scales, to better understand fabric orientation in specific tectonic domains.

REFERENCES

Abramson, E. H., Brown, J. M., Slutsky, L. J., & Zaug, J., 1997. The elastic constants of San Carlos olivine to 17 GPa, *Journal of Geophysical Resarch*, **102**(B6), 12,253–12,263.

Babuska, V. & Cara, M., 1991. Introduction, in *Seismic Anisotropy in the Earth*, chap. 1, pp. 1–3, eds Kennett, B. L. N., Madariaga, R., Marschall, R., & Wortel, R., Springer.

Barruol, G., Bonnin, M., Pedersen, H., Bokelmann, G. H. R., & Tiberi, C., 2011. Belt-parallel mantle flow beneath a halted continental collision: The Western Alps, *Earth and Planetary Science Letters*, **302**, 429–438.

Berens, P., 2009. CircStat: A MATLAB Toolbox for Circular Statistics, *Journal of Statistical Software*, **31**(10), 1–21.

Bokelmann, G., Qorbani, E., & Bianchi, I., 2013. Seismic anisotropy and large-scale deformation of the Eastern Alps, *Earth and Planetary Science Letters*, **383**, 1–6.

Bokelmann, G. H. R., 2002a. Convection-driven motion of the North American craton: Evidence from P-wave anisotropy, *Geophysical Journal International*, **148**(2), 278–287.

Bokelmann, G. H. R., 2002b. Which forces drive North America?, *Geology*, (11), 1027.

Bokelmann, G. H. R. & Silver, P. G., 2000. Mantle variation within the Canadian Shield: Travel times from the portable broadband Archean-Proterozoic Transect 1989, *Journal of Geophysical Research*, **105**(B1), 579–605.

Browaeys, J. & Chevrot, S., 2004. Decomposition of the elastic tensor and geophysical applications, *Geophysical Journal International*, **159**(2), 667–678.

Crotwell, H. P., Owens, T. J., & Ritsema, J., 1999. The TauP Toolkit: Flexible seismic travel-time and ray-path utilities, *Seismological Research Letter*, **70**(2), 154–160.

Davis, P. M., 2003. Azimuthal variation in seismic anisotropy of the southern California uppermost mantle, *Journal of Geophysical Research: Solid Earth*, **108**(B1), 24–1 – 24–18.

Eakin, C. M., Obrebski, M., Allen, R. M., Boyarko, D. C., Brudzinski, M. R., & Porritt, R., 2010. Seismic anisotropy beneath Cascadia and the Mendocino triple junction: Interaction of the subducting slab with mantle flow, *Earth and Planetary Science Letters*, **297**, 627–632.

Faccenda, M. & Capitanio, F., 2013. Seismic anisotropy around subduction zones: Insights from three-dimensional modeling of upper mantle deformation and SKS splitting calculations, *Geochemistry, Geophysics, Geosystems*, **14**(1), 243–262.

Hielscher, R. & Schaeben, H., 2008. A novel pole figure inversion method: specification of the MTEX algorithm, *Journal of Applied Crystallography*, **41**, 1024–1037.

Hongsresawat, S., Panning, M. P., Russo, R. M., Foster, D. A., Monteiller, V., & Chevrot, S., 2015. USArray shear wave splitting shows seismic anisotropy from both lithosphere and asthenosphere, *Geology*, **43**(8), 667–670.

IRIS DMC, 2014. Data Services Products: SWS-DB-MST The Missouri S&T western and central United States shear-wave splitting database, `http://ds.iris.edu/ds/products/sws-db-mst/`.

Karato, S.-I., 2008. Seismic anisotropy and its geodynamic implications, in *Deformation of Earth Materials - An Introduction to the Rheology of Solid Earth*, chap. 21, pp. 391–411, Cambridge University Press, Cambridge, 1st edn.

Liu, K. H., Elsheikh, A., Lemnifi, A., Purevsuren, U., Ray, M., Refayee, H., Yang, B. B., Yu, Y., & Gao, S. S., 2014. A uniform database of teleseismic shear wave splitting measurements for the western and central United States, *Geochemistry, Geophysics, Geosystems*, **15**(5), 2075–2085.

Long, M. D. & Silver, P. G., 2008. The Subduction Zone Flow Field from Seismic Anisotropy: A Global View, *Science*, **319**(5861), 315–318.

Mainprice, D., 1990. A FORTRAN program to calculate seismic anisotropy from the lattice preferred orientation of minerals, *Computers & Geosciences*, **16**(3), 385–393.

Mainprice, D., 2014. Single Crystal Physical Properties databases (Unicef Carebases), `www.gm.univ-montp2.fr/PERSO/mainprice/`, Université de Montpellier.

Mainprice, D., 2015. Seismic Anisotropy of the Deep Earth from a Mineral and Rock Physics Perspective, in *Treatise on Geophysics*, chap. 2.20, pp. 487–538, ed. Schubert, G., Elsevier B.V., 2nd edn.

Mainprice, D., Barruol, G., & Ismaïl, W. B., 2000. The Seismic anisotropy of the Earth's mantle: From single crystal to polycrystal, in *Earth's Deep Interior: Mineral Physics and Tomography From the Atomic to the Global Scale*, chap. 11, pp. 237–264, eds Karato, S., Forte, A., Liebermann, R., Masters, G., & Stixrude, L., American Geophysical Union.

McDonough, W. F. & Rudnick, R. L., 1998. Mineralogy and composition of the upper mantle, *Reviews in Mineralogy and Geochemistry*, **37**(1), 139–164.

Menke, W. & Levin, V., 2003. The cross-convolution method for interpreting SKS splitting observations, with application to one and two-layer anisotropic earth models, *Geophysical Journal International*, **154**(2), 379–392.

Nicolas, A. & Christensen, N. I., 1987. Formation of Anisotropy in Upper Mantle Peridotites - A Review, in *Composition, Structure and Dynamics of the Lithosphere-Asthenosphere System, Volume 16*, pp. 111–123, eds Fuchs, K. & Froidevaux, C., American Geophysical Union.

NOAA NCEI, 2013. ETOPO1 Global Relief Model, `https://www.ngdc.noaa.gov/mgg/global/global.html`.

Özalaybey, S. & Savage, M. K., 1995. Shear-wave splitting beneath western United States in relation to plate tectonics, *Journal of Geophysical Research: Solid Earth*, **100**(B9), 18135–18149.

Qorbani, E., Bianchi, I., & Bokelmann, G., 2015. Slab detachment under the Eastern Alps seen by seismic anisotropy, *Earth and Planetary Science Letters*, **409**, 96–108.

Savage, M. K. & Sheehan, A. F., 2000. Seismic anisotropy and mantle flow from the Great Basin to the Great Plains, western United States, *Journal of Geophysical Research*, **105**(B6), 715–728.

Savage, M. K. & Silver, P. G., 1993. Mantle deformation and tectonics: constraints from seismic anisotropy in the western United States, *Physics of the Earth and Planetary Interiors*, **78**(3-4), 207–227.

Silver, P. G., 1996. Seismic Anisotropy Beneath the Continents: Probing the Depths of Geology, *Annual Review of Earth and Planetary Sciences*, **24**(1), 385–432.

Silver, P. G. & Chan, W. W., 1988. Implications for continental structure and evolution from seismic anisotropy, *Nature*, **335**(6185), 34–39.

Silver, P. G. & Chan, W. W., 1991. Shear wave splitting and subcontinental mantle deformation, *Journal of Geophysical Research*, **96**(B10), 16429–16454.

Song, T. A. & Kawakatsu, H., 2012. Subduction of oceanic asthenosphere: Evidence from sub-slab seismic anisotropy, *Geophysical Research Letter*, **39**(L17301), 1–6.

Soustelle, V., Tommasi, A., Demouchy, S., & Ionov, D. A., 2010. Deformation and Fluidˆ Rock Interaction in the Supra-subduction Mantle: Microstructures and Water Contents in Peridotite Xenoliths from the Avacha Volcano, Kamchatka, *Journal of Petrology*, **51**(1 & 2), 363ˆ394.

Vinnik, L. P., Kosarev, G. L., & Makeyeva, L. I., 1984. Anisotropy of the lithosphere from the observation of SKS and SKKS, *Proceedings of the Academy of Sciences of USSR*, **278**, 1335–1339.

Vinnik, L. P., Farra, V., & Romanowicz, B., 1989. Azimuthal anisotropy in the earth from observations of SKS at GEOSCOPE and NARS broadband stations, *Bulletin of the Seismological Society of America*, **79**(5), 1542–1558.

Walker, A. & Wookey, J., 2012. MSAT — A new toolkit for the analysis of elastic and seismic anisotropy, *Computers and Geosciences*, **49**, 81–90.

Wookey, J. & Walker, A., 2015a. Modelling shear-wave splitting variation with backazimuth, `https://www1.gly.bris.ac.uk/MSAT/doc/examples/splitting_model_example.html`, University of Bristol.

Wookey, J. & Walker, A., 2015b. Shear wave splitting, `https://www1.gly.bris.ac.uk/MSAT/doc/MSATfunctions.html`, University of Bristol.

Wookey, J. & Walker, A., 2015c. MS_norms - Browaeys and Chevrot analysis of the elasticity matrix, `https://www1.gly.bris.ac.uk/MSAT/doc/funcs/MS_norms.html`, University of Bristol.

Wüstefeld, A. & Bokelmann, G., 2007. Null Detection in Shear-Wave Splitting Measurements, *Bulletin of the Seismological Society of America*, **97**(4), 1204–1211.

Wüstefeld, A., Bokelmann, G., Zaroli, C., & Barruol, G., 2008. SplitLab: A shear-wave splitting environment in Matlab, *Computers & Geosciences*, **34**(5), 515–528.

Yang, B. B., Gao, S. S., Liu, K. H., Elsheikh, A. A., Lemnifi, A. A., Refayee, H. A., & Yu, Y., 2014. Seismic anisotropy and mantle flow beneath the northern Great Plains of North America, *Journal of Geophysical Research: Solid Earth*, **119**(3), 1971–1985.

Yuan, H. & Romanowicz, B., 2010. Depth dependent azimuthal anisotropy in the western US upper mantle, *Earth and Planetary Science Letters*, **300**(3-4), 385–394.

Yuan, H., Romanowicz, B., Fischer, K. M., & Abt, D., 2011. 3-D shear wave radially and azimuthally anisotropic velocity model of the North American upper mantle, *Geophysical Journal International*,

184, 1237–1260.

Figures

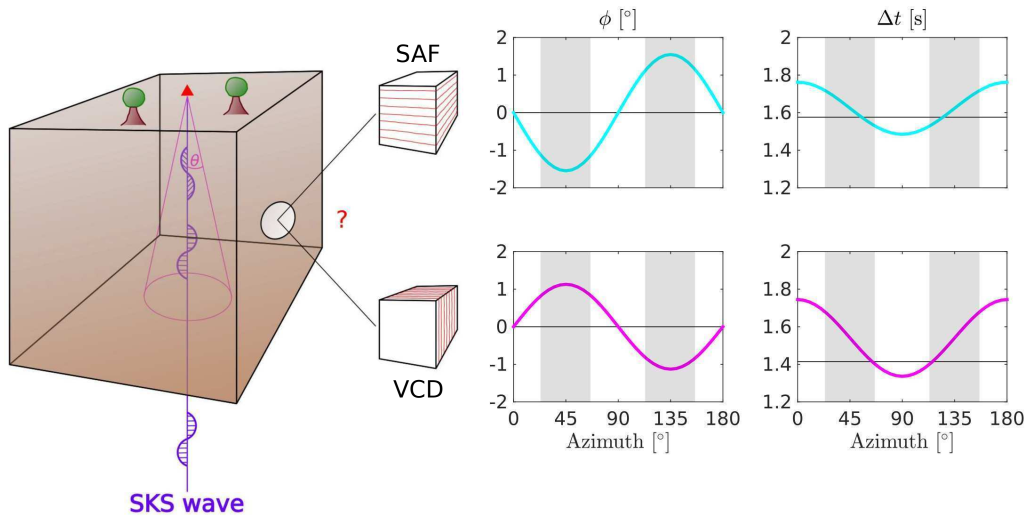

Figure 1. (left) Ray geometry of SKS waves, along a cone through the upper mantle under the seismological station. (center) The two endmember models of geodynamic interest, the Simple Asthenospheric Flow Model (above), associated with a horizontal orientation of foliation planes, and the Vertical Coherent Deformation (below), associated with a steep orientation of foliation planes. (right) Expected azimuthal variations of shear-wave splitting parameters (fast orientations ϕ and delay times Δt) for the two models in comparison to a vertical incidence case (black lines), assuming, for the sake of simplicity, a mantle consisting of pure olivine [70 % b-up (top, cyan lines) or c-up (bottom, magenta lines) and 30 % isotropic]. Note that the azimuthal variation is rather different i.p. around extrema of ϕ (gray shaded intervals), depending on the orientation of the crystals.

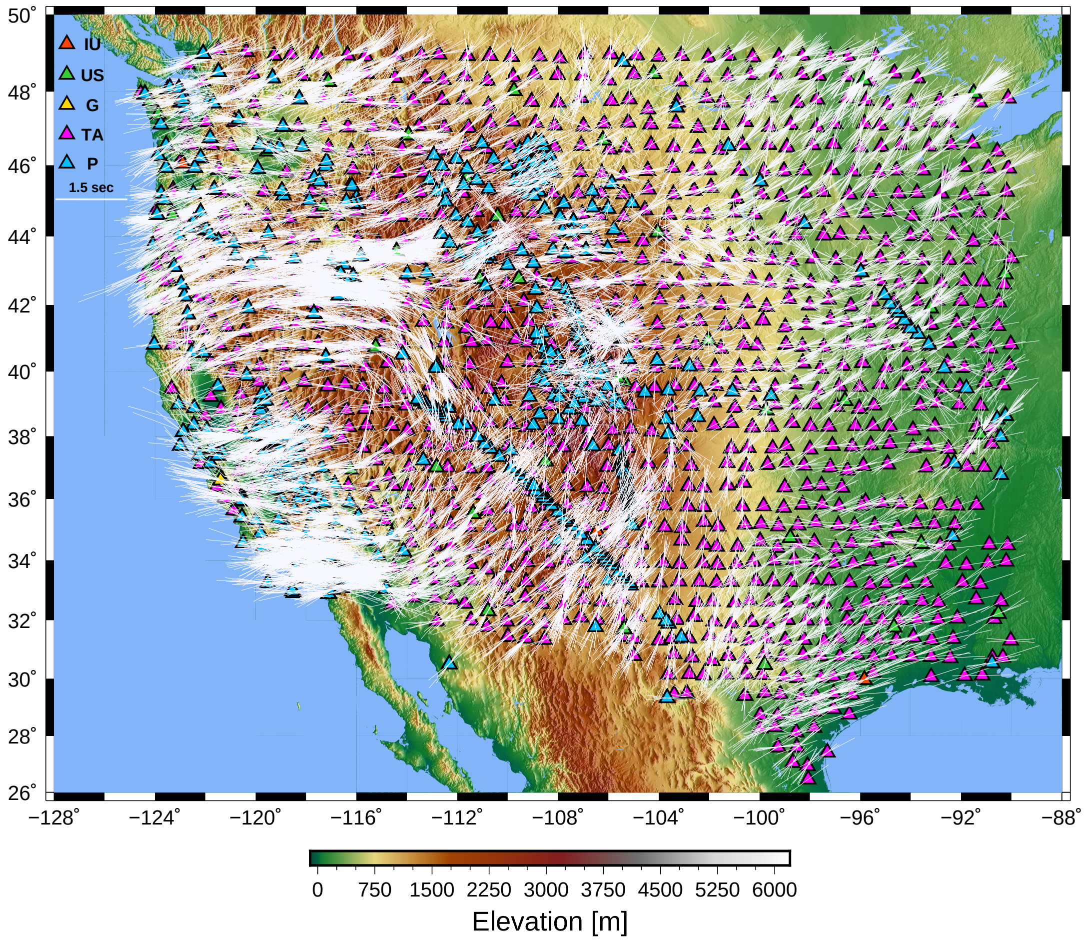

Figure 2. Individual fast orientations ϕ of the shear-wave splitting dataset SWS-DB-MST from Liu et al. (2014). Lengths of the lines show the delay times Δt. Network abbreviations are given in the text.

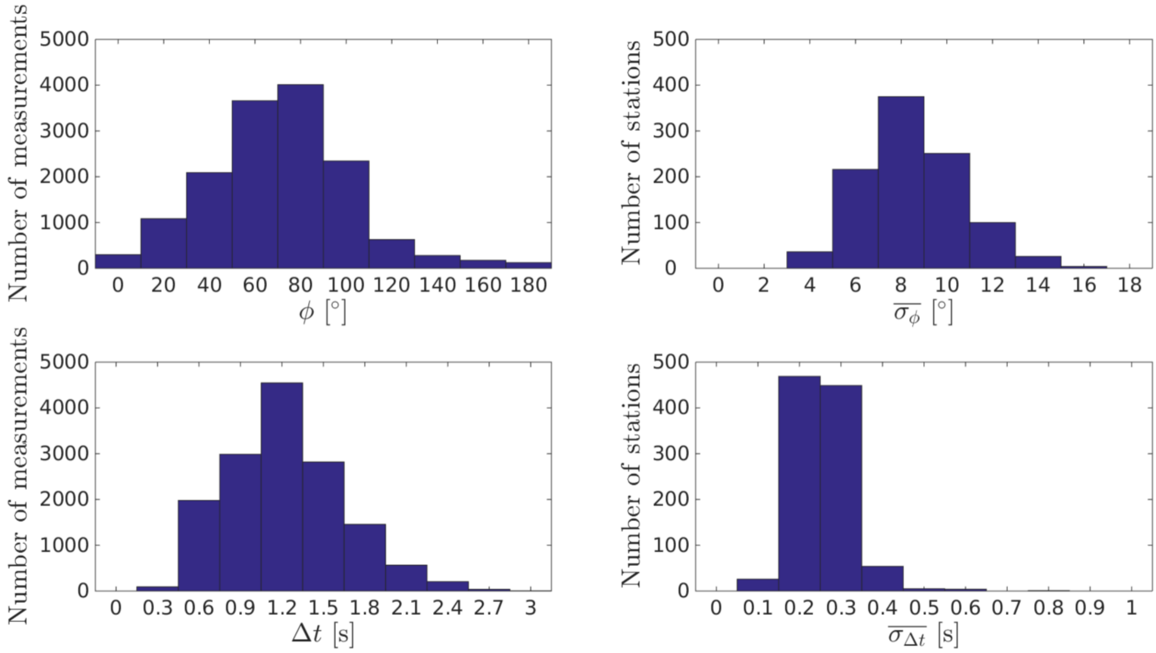

Figure 3. Histograms of shear-wave splitting parameters and their uncertainties. (left) Number of measurements per fast orientation ϕ (top) and delay time Δt (bottom) interval. (right) Number of stations per bin of $\overline{\sigma}$, the mean standard deviation of ϕ and Δt per station. In terms of stability, only stations with at least five measurements are considered.

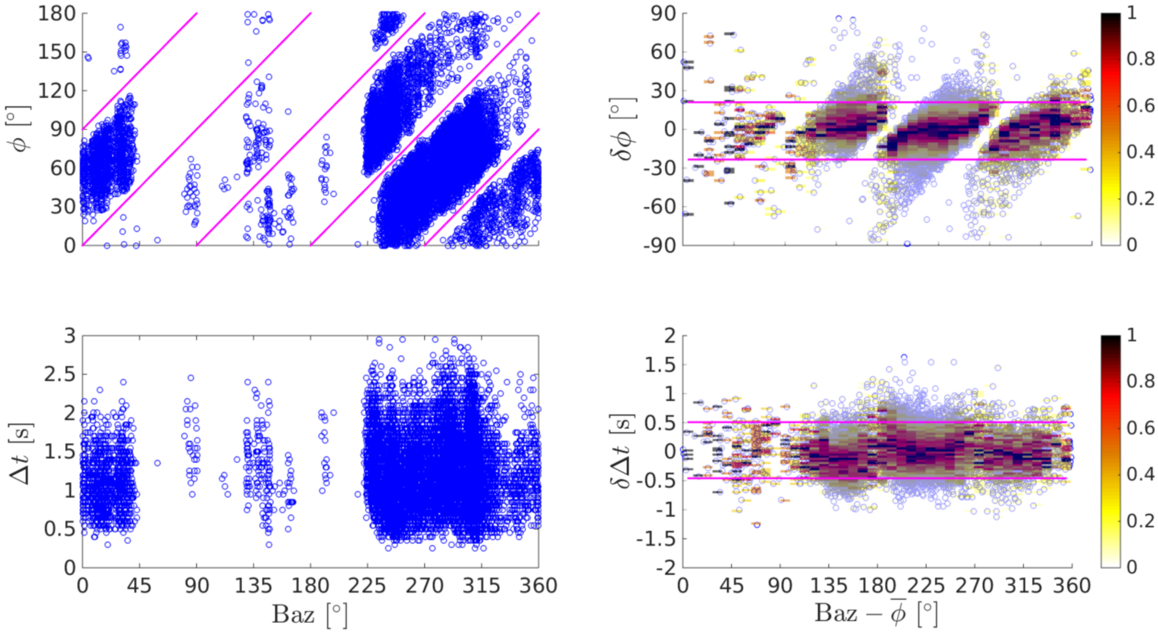

Figure 4. Backazimuthal (Baz) distribution of individual shear-wave splitting parameters. (left) Fast orientations ϕ and delay times Δt from all SKS and SKKS arrivals (magenta lines: Null directions). (right) Overlay of variations $\delta\phi$ and $\delta\Delta t$ (from station averages) corrected for the different fast orientation per station $\overline{\phi}$ (selected stations have at least five observations), and their relative frequency (per bin of $\sim 8.95\,° \times 2.19\,°$ and $\sim 8.95\,° \times 0.04\,$s; magenta lines: thresholds of 5 % and 95 % quantile, see text).

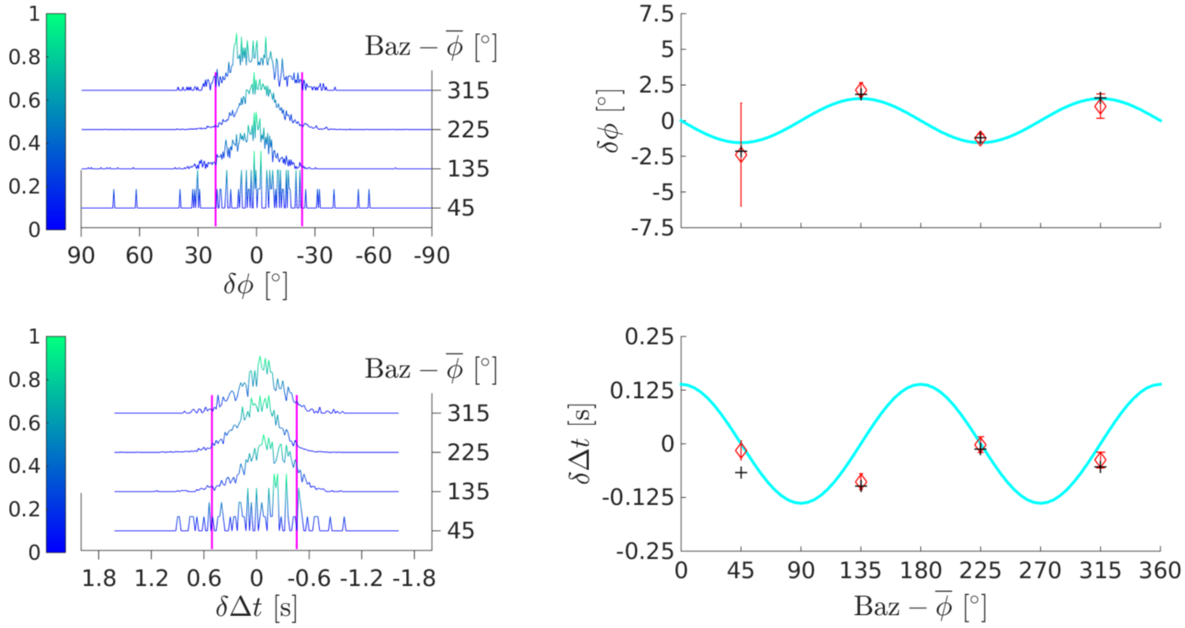

Figure 5. Backazimuthal (Baz) changes of shear-wave splitting parameters. (left) Relative frequencies of selected fast orientation and delay time variation, $\delta\phi$ and $\delta\Delta t$ (inside interval of $\pm 15\,^\circ$; per bin of $0.5\,^\circ \times 30\,^\circ$ and $0.02\,\mathrm{s} \times 30\,^\circ$; magenta lines: thresholds of $5\,\%$ and $95\,\%$ quantile). (right) Derived mean (diamond), median (plus) and 2σ-error of the mean $\delta\phi$ and $\delta\Delta t$ in comparison with expected variations (cyan line) from the Taylor-series expansion of Fig. 1 (top right) for a b-up olivine orientation.

T domains	Dominant slip systems	Relation with flow plane (horizontal) and flow line (arrow)	Value of the oscillation parameter d_1
≥ 1250°C (hypersolidus)	(010) [100] (001) [100]	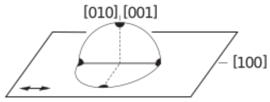	~ 0 depends on relative volume fraction
> 1100°C (high-T)	(010) [100]	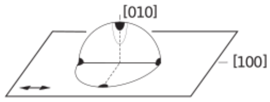	**< 0**
~ 1000°C (medium-T)	(0kl) [100]	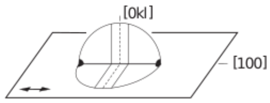	~ 0
700 - 1000°C (low-T)	(0kl) [100] (010) [001]	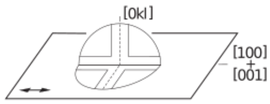	~ 0

Figure 6. Olivine slip systems and flow orientations for the upper mantle (after Nicolas & Christensen 1987). The column of the right gives the predicted value of the oscillation parameter d_1.

APPENDIX A: CALCULATION OF AZIMUTHAL VARIATION

To verify the findings from the non-vertical SWS approach, we compare the Taylor-series expansion to the full (numerical) solution (Mainprice 1990) implemented in MSAT (Wookey & Walker 2015a). For simplicity we asssume a horizontal single-layer case of anisotropy (70 % San Carlos olivine b-up or c-up) between 0 km − 100 km, oriented towards north, and set $\theta \sim 11.23\,^{\circ}$. The related stiffness tensor (Eq. A.1) is shown in Eq. A.2 (b-up) and Eq. A.3 (c-up) in GPa.

$$C_{ijkl} = \begin{bmatrix} C_{1111} & C_{1122} & C_{1133} & 0 & 0 & 0 \\ C_{1122} & C_{2222} & C_{2233} & 0 & 0 & 0 \\ C_{1133} & C_{2233} & C_{3333} & 0 & 0 & 0 \\ 0 & 0 & 0 & C_{2323} & 0 & 0 \\ 0 & 0 & 0 & 0 & C_{1313} & 0 \\ 0 & 0 & 0 & 0 & 0 & C_{1212} \end{bmatrix} \tag{A.1}$$

$$\begin{aligned} &C_{1111} = 292.01,\ C_{1122} = 73.87, \\ &C_{1133} = 71.02,\ C_{2222} = 234.69, \\ &C_{2233} = 77.29,\ C_{3333} = 207.95, \\ &C_{2323} = 68.32,\ C_{1313} = 78.95, \\ &C_{1212} = 77.75 \end{aligned} \tag{A.2}$$

$$\begin{aligned} &C_{1111} = 292.01,\ C_{1122} = 71.02, \\ &C_{1133} = 73.87,\ C_{2222} = 207.95, \\ &C_{2233} = 77.29,\ C_{3333} = 234.69, \\ &C_{2323} = 68.32,\ C_{1313} = 77.75, \\ &C_{1212} = 78.95 \end{aligned} \tag{A.3}$$

Both the Taylor-series expansion and the full solution show oscillations in the azimuthal distribution of the SWS parameters for non-vertical ray path incidence (Fig. A1), and the opposite polarity of ϕ (top) for the b-up and the c-up case. The amplitude of the variation are not identical, but they agree to first order, sufficiently well for our study. Considering the expected Δt (bottom) amplitude, both foliation orientation vary only slightly, analogous to the Taylor-series expansion. As this Δt differences are not significant enough to distinguish between the two cases, we favor the relation of the phase information of ϕ and the d_1 polarity as criteria.

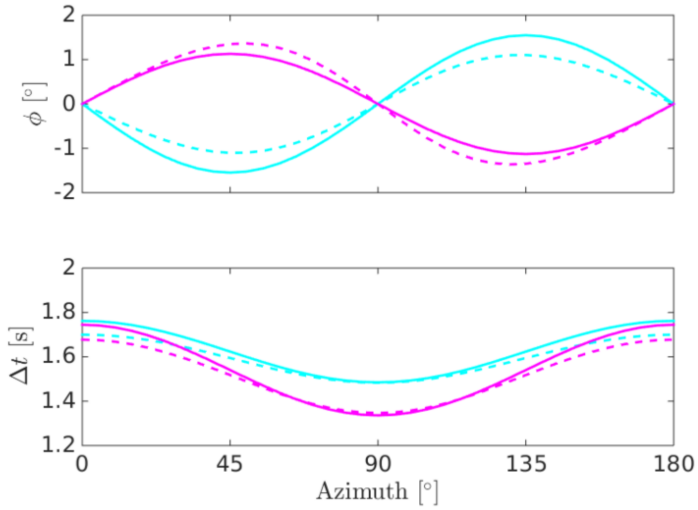

Figure A1. Synthetic test comparing non-vertical shear-wave splitting solutions for a single-layer anisotropy case of b-up (cyan) and c-up (magenta) olivine (elastic constants/model parameters see text). The numerical solution (dashed lines) and the Taylor-series expansion (solid lines) of the Christoffel equation predict similar backazimuthal variations of ϕ (top) and Δt (bottom) respectively, to first order.

APPENDIX B: INFLUENCE OF THE AMOUNT OF OLIVINE

For the sake of the argument, our investigation assumes a simplified upper mantle model composed of 70 % aligned olivine. The true percentage of similar orientation is not known. We thus determine the effect of the percentage of aligned olivine on d_1 and e_2 in Fig. A2. Additionally the change in anisotropy strength is determined by comparing the matrix norm, related to the anisotropic stiffness tensor, with its isotropic equivalent (see MSAT implementation of Wookey & Walker 2015c based on Browaeys & Chevrot 2004).

Varying the amount of olivine from 30 % (see e.g. Davis 2003) to 70 % only slightly changes d_1 (top) for both orientations (30 %: $d_{1b} \sim -0.69$, $d_{1c} \sim 0.49$; 70 %: $d_{1b} \sim -0.7$, $d_{1c} \sim 0.51$), however e_2 (bottom) is more influenced (30 %: $e_{2b} \sim 1.32$, $e_{2c} \sim 2$; 70 %: $e_{2b} \sim 3.61$, $e_{2c} \sim 5.32$). A higher percentage of olivine particularly leads to larger amplitudes in $\delta\Delta t$, but does not significantly change $\delta\phi$. Increasing the amount of olivine further raises the strengh of anisotropy from $\sim$ 5.29 % to 12.61 %, indicating a tendency to overestimate the strength of upper mantle anisotropy. However, our calculation of the percentage of anisotropy directly from the stiffness tensor is rather suitable to characterize single-crystal anisotropy, the actual strength of anisotropy in terms of Δt is not only effected by the compositon itself. The tradeoff with the layer thickness and the related path length is obvious. Similarly as the composition, the layer thickness is not known accurately, but as Fig. A1 indicates that our model generates resonable Δt values, we assume the combination of 70 % olivine and 100 km thickness to be sufficiently appropriate for our investigation. Future studies might consider the effect of more complex models, taking e.g. orthopyroxene in different orientations into account, what will have an additional influence on d_1 and e_2.

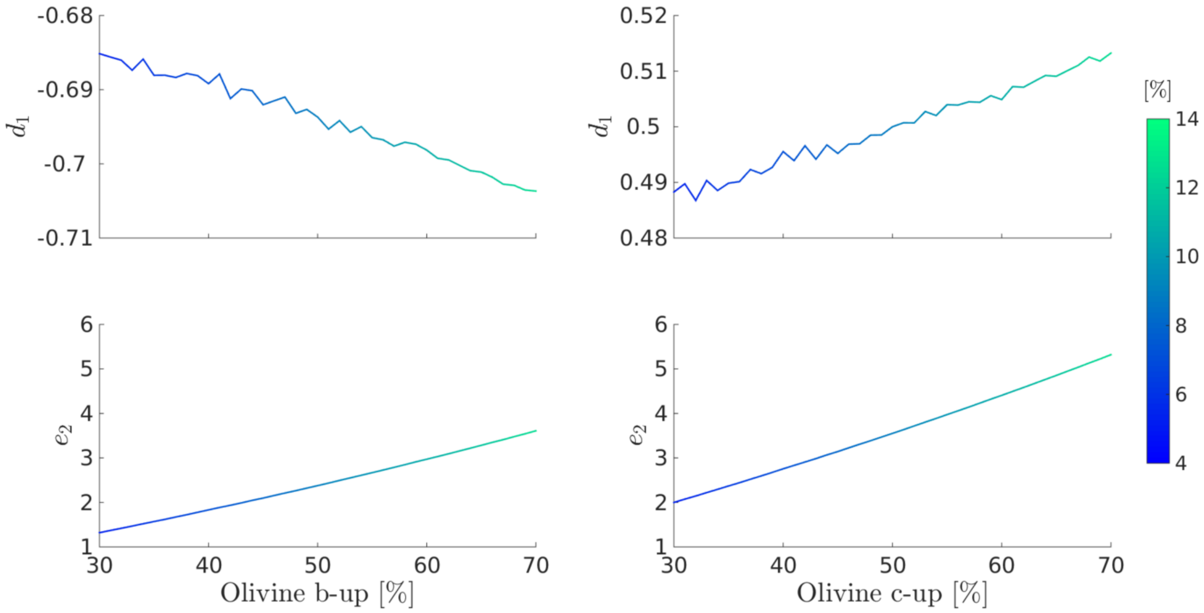

Figure A2. Variation of the d_1 (top) and e_2 (bottom) parameter with changing amounts of aligned olivine in a b-up (left) and c-up (right) orientation of the model in Appendix A. The colorbar indicates the anisotropy percentage (see text for explanation).

APPENDIX C: THRESHOLD COMBINATIONS

The following Fig. A3 illustrates that slight changes in the choice of our thresholds do not significantly change the outcome. The overall good fit between expected and observation-derived variations remains stable.

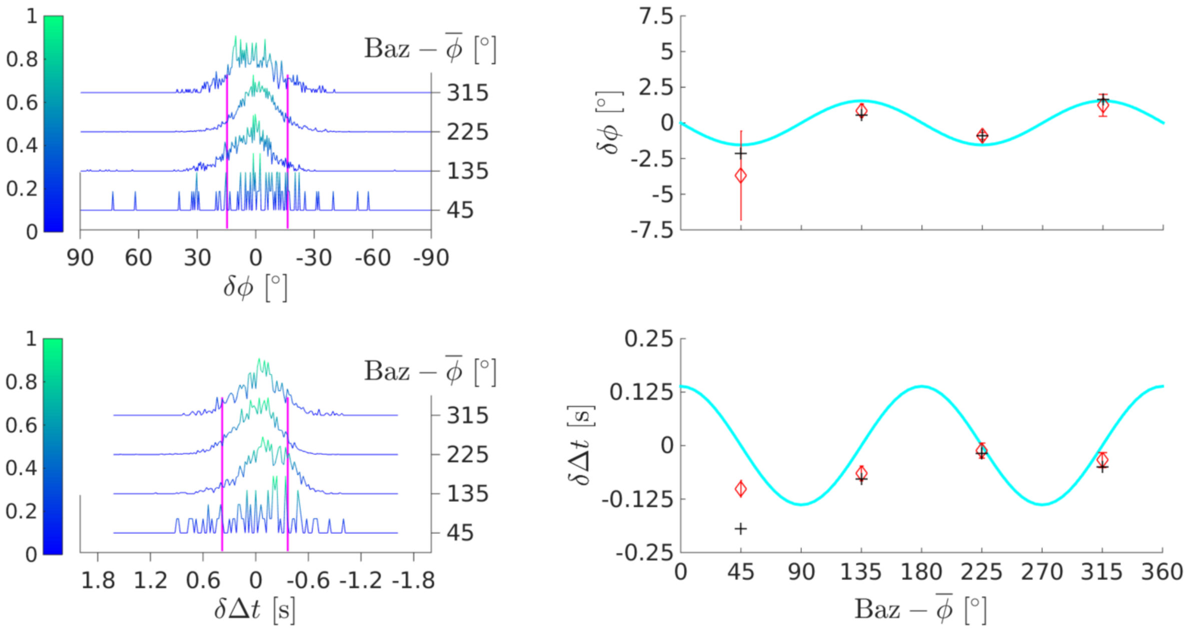

Figure A3. Backazimuthal (Baz) changes of shear-wave splitting parameters. (left) Relative frequencies of selected fast orientation and delay time variation, $\delta\phi$ and $\delta\Delta t$ (inside interval of $\pm 15\,^\circ$; per bin of $0.5\,^\circ \times 30\,^\circ$ and $0.02\,\mathrm{s} \times 30\,^\circ$; magenta lines: thresholds of 10 % and 90 % quantile). (right) Derived mean (diamond), median (plus) and 2σ-error of the mean $\delta\phi$ and $\delta\Delta t$ in comparison with expected variations (cyan line) from the Taylor-series expansion of Fig. 1 (top right) for a b-up olivine orientation.

APPENDIX D: ROBUSTNESS OF THE NON-VERTICAL SHEAR-WAVE SPLITTING PROCEDURE

Since actual SWS measurements can be affected by various factors, e.g. noisy conditions and specific side characteristics, the robustness of our procedure can be evaluated best during a synthetic test. Here we generate 100 stations above a single-layer of b-up olivine with a constant layer thickness of 100 km. As in Appendix A, we determine the predicted SWS backazimuth distribution for a constant incidence angle of $\sim 11.23\,°$, but this time the lateral orientation of the olivine a-axis is randomly defined between $[-90\,°, 90\,°]$.

After the forward modeling the number and backazimuths of synthetic measurements is determined randomly per station. Taking advantage of the splitting functions already implemented in MSAT (Wookey & Walker 2015b), we generate a pair of signals for each chosen backazimuth source polarisation, add Gaussian noise to each component, and normalize them to the maximum of both traces. Subsequently we simulate the splitting of both time series at a station based on the SWS parameters we predicted for this situation at the beginning. Running a grid search (spacing: $0.25\,°$; $0.125\,$s) the restored SWS parameters vary from the prediction. Following our procedure, we transfer ϕ to $[0\,°, 180\,°]$, calculate $\overline{\phi}$ and $\overline{\Delta t}$, the means per station, and determine $\delta\phi$, $\delta\Delta t$ for $\overline{\phi}$ corrected backazimuths. After 10 stations we estimate the mean, median and error of the mean of $\delta\phi$ and $\delta\Delta t$ per interval and defined thresholds (see main text), and repeat the procedure.

Figure A4 shows the backazimuthal distribution of ϕ (top) and Δt (bottom) for all 100 stations of single-layer anisotropy with a b-up olivine and variable a-axis orientation for non-vertical SWS arrivals. While ϕ varies across the whole range from $\sim 0\,°$ to $180°$, Δt is mainly concentrated between $\sim 1.5\,$s to $1.75\,$s. The overall backazimuthal coverage is consistent and very wide. Following our procedure to calculate $\delta\phi$ (top right) and $\delta\Delta t$ (bottom right) by shifting the individual synthetic measurements according to $\overline{\phi}$ and $\overline{\Delta t}$, we are able to restore the typical $180\,°$ periodicity for a b-up olivine situation even though the initial time series were disturbed. As a consequence the determined $\overline{\delta\phi}$ and $\overline{\delta\Delta t}$ are also in very good agreement with the predicted trend.

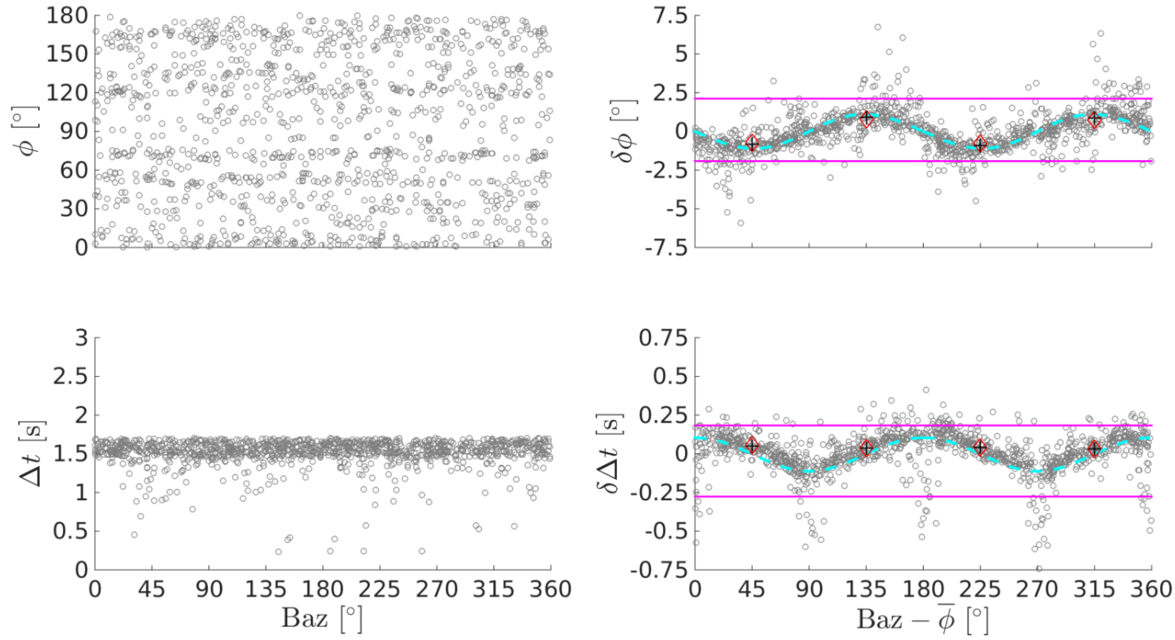

Figure A4. Backazimuthal (Baz) distribution of individual synthetic shear-wave splitting parameters. (left) Fast orientations ϕ (top) and delay times Δt (bottom) are determined for simulated non-vertical arrivals of SKS phases, passing through a single-layer of b-up olivine with a randomly determined a-axes orientation. (right) Zoom into the variations $\delta\phi$ and $\delta\Delta t$ (from station averages) corrected for the different fast orientation per station $\overline{\phi}$. The derived mean (diamond) and median (plus) of $\delta\phi$ and $\delta\Delta t$ of selected values (inside interval of $\pm 15\,°$; magenta lines: thresholds of 5% and 95% quantile) are shown in comparison with the expected variations (dashed, cyan line) from the numerical solution in Fig. A1 for a b-up olivine orientation.

Figure A5 indicates the decreasing behavior of the minimum, mean and maximum of the error of the mean with an increasing number of synthetic measurements inside the intervals and thresholds. This concerns 306 pairs of SWS parameters from an overall number of 1168 measurements at 100 stations. The fact that the error finally reaches a range between $\sim 0.15\,°$ to $0.19\,°$ and ~ 0.01 s confirms that our method is able to robustly resolve the expected small $\delta\phi$ and $\delta\Delta t$ variations.

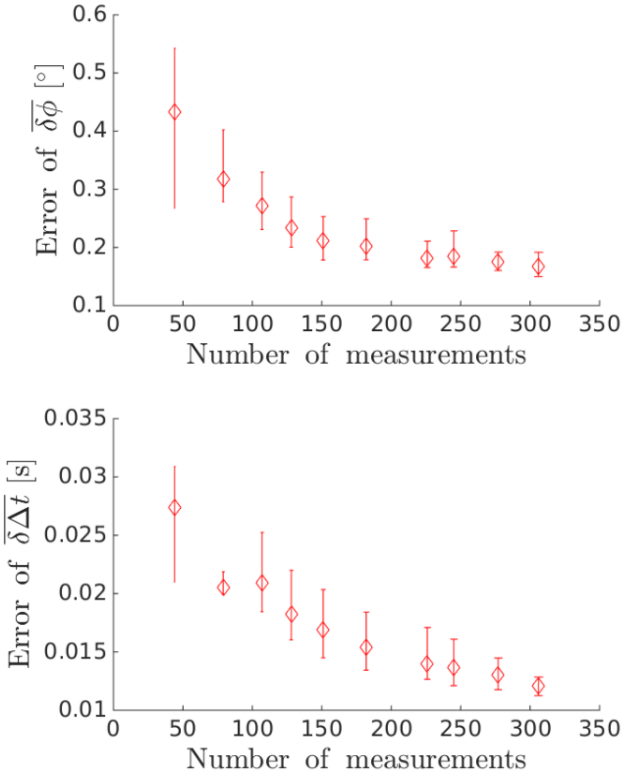

Figure A5. Development of the error of $\overline{\delta\phi}$ (top) and $\overline{\delta\Delta t}$ (bottom) with an increasing number of selected individual synthetic splitting measurements (inside interval of $\pm 15\,^{\circ}$; thresholds of 5% and 95% quantile). The mean (diamond), maximum (top edge) and minimum (bottom edge) error is determined after every 10 stations.

APPENDIX E: INCIDENCE DEPENDENCE OF $\delta\phi$

One might wonder whether the new measure is really sensitive to both mantle lithosphere and asthenosphere due to potentially differing incidence angles. We tested this using the PREM model and TauP (Crotwell et al. 1999), and we determined the depth dependence of θ for a median epicentral distance of $\sim 96.4\,^\circ$ and focal-depth of 57 km considering only SKS phases of the dataset in Fig. A6 (top). Assuming (for the sake of the argument) a constant d_1 for each foliation orientation ($d_{1b} \sim -0.7; d_{1c} \sim 0.51$) in crust and upper mantle, we calculated the related maximum of $\delta\phi$ for different depths. As shown in Fig. A6 (bottom), due to steeper ray path incidence in the crust (smaller θ), the amplitude of $\delta\phi$ decreases in this depth range, while it is nearly constant in the upper mantle. We can thus conclude that the effect is sensitive to the entire upper mantle, including mantle lithosphere and asthenosphere. This conclusion holds similarly for the azimuthal variations of the SWS delay which is not shown specifically in Fig. A6.

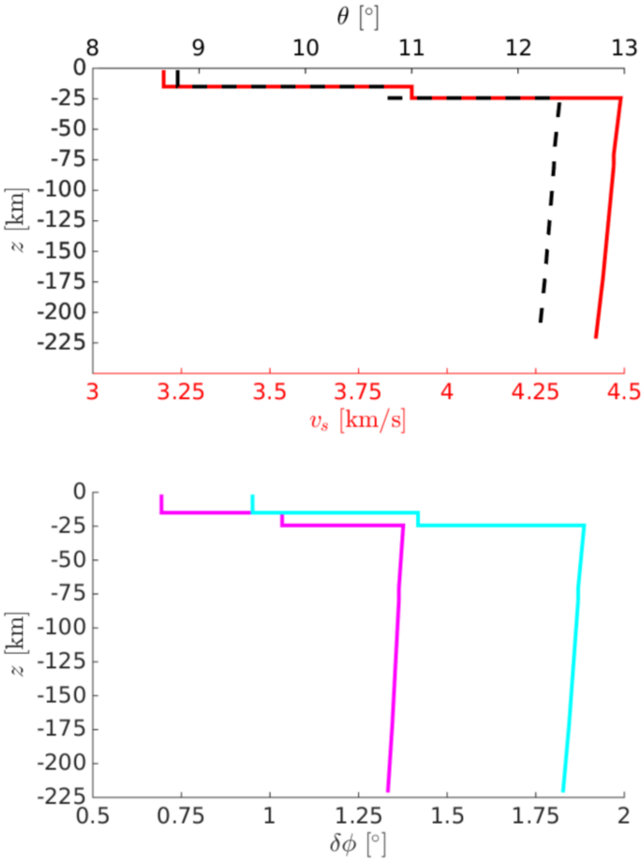

Figure A6. (top) Incidence angle dependence on depth (black, dashed line) for the PREM velocity model (red line). (bottom) Amplitude of azimuthal variation as a function of depth, for the two cases b-up (cyan) and c-up (magenta).

APPENDIX F: $\delta\phi$ AND $\delta\Delta T$ OF HIGH-QUALITY STATIONS

The non-vertical SWS approach only considers horizontal single-layer anisotropy, but e.g. dipping layer or multiple-layer anisotropy cases could bias our results. To test whether our findings are mainly related to non-vertical incidence, we take advantage of the suggestion of Liu et al. (2014) that the distribution of areas of increased complexity of anisotropy correlates with regions of higher standard deviations. We therefore introduce a threshold for $\overline{\sigma_\phi}$, based on the related distribution, to further preselect stations and apply our procedure again. The results for high-quality stations inside the 75 % quantile of $\overline{\sigma_\phi}$ unveil (Fig. A7) similar distributions of relative frequencies and the general backazimuthal variation for $\delta\phi$ and $\delta\Delta t$ as in Fig. 5 of the main text.

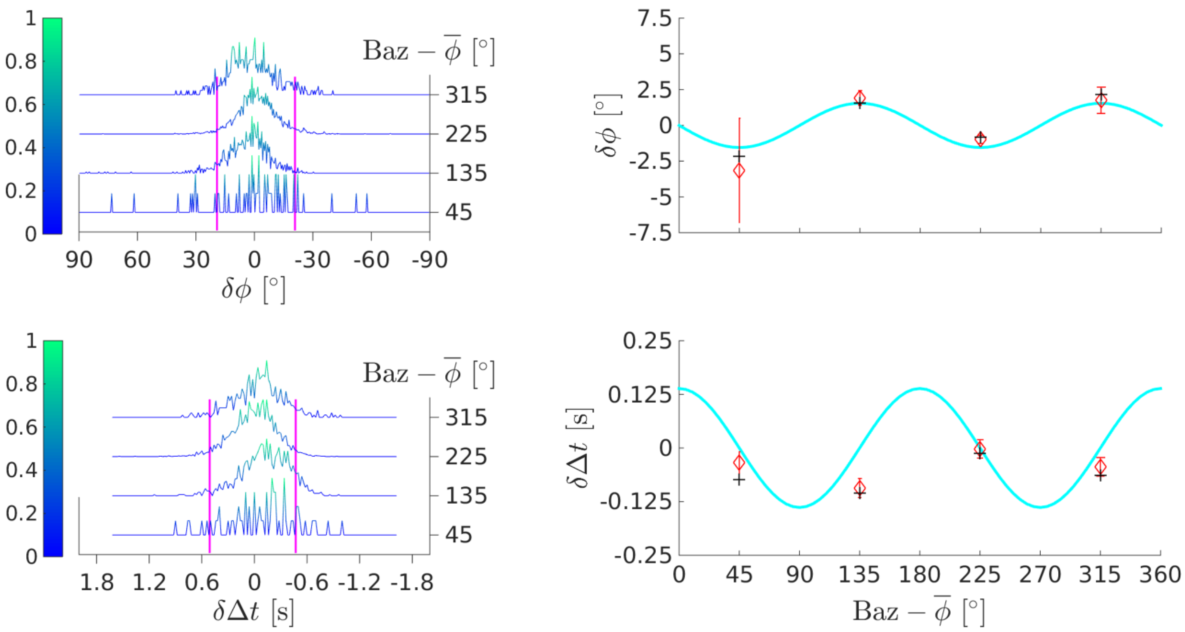

Figure A7. Backazimuthal (Baz) changes of shear-wave splitting parameters (high-quality stations within 75 % quantile of $\overline{\sigma_\phi}$). (left) Relative frequencies of selected fast orientation and delay time variation, $\delta\phi$ and $\delta\Delta t$ (inside interval of $\pm 15\,°$; per bin of $0.5\,° \times 30\,°$ and $0.02\,\mathrm{s} \times 30\,°$; magenta lines: thresholds of 5 % and 95 % quantile). (right) Derived mean (diamond), median (plus) and 2σ-error of the mean $\delta\phi$ and $\delta\Delta t$ in comparison with expected variations (cyan line) from the Taylor-series expansion of Fig. 1 (top right) for a b-up olivine orientation.

ACKNOWLEDGMENTS

We want to thank Ehsan Qorbani for his comments on an early version of this manuscript. This work has profited from the IRIS/USGS Global Seismographic Network (10.7914/SN/IU), the US National Seismic Network (10.7914/SN/US), the USArray Transportable Array (10.7914/SN/TA), the GEOSCOPE (10.18715/GEOSCOPE) and PASSCAL initiatives, serving as a basis for the SWS database put online by Liu et al. (2014), and hosted by IRIS DMC (2014) - and the topographic map provided by NOAA NCEI (2013), the MTEX elastic tensor database maintained by Mainprice (2014) as well as the MSAT, CircStat and TauP functions implemented by Walker & Wookey (2012), Berens (2009) and Crotwell et al. (1999) respectively. Part of this work was supported by the Austrian Science Fund FWF Projects Number P26391 and P30707.

Corresponding author: E. Löberich, eric.loeberich@univie.ac.at